jntes

JOURNAL OF NEW TECHNOLOGIES IN ENVIRONMENTAL SCIENCE

3

2023

No. 3 Vol. 7 ISSN 2544-7017 www.jntes.tu.kielce.pl Kielce University of Technology

CONTENTS

www.jntes.tu.kielce.pl
jntes@tu.kielce.pl

The quarterly printed issues of Journal of New Technologies in Environmental Science are their original versions. The Journal published by the Kielce University of Technology.

ISSN 2544-7017

Doi: 10.53412

jntes
3
2023

Borys BASOK, Svitlana GONCHARUK
Maryna MOROZ, Hanna VEREMIICHUK
Institute of Engineering Thermophysics National Academy of Sciences of Ukraine, Kyiv, Ukraine
Corresponding author: morozmarina234@gmail.com

Doi: 10.53412/jntes-2023-3-1

EXPERIMENTAL RESEARCH OF HEAT TRANSFER THROUGH HEAT-INSULATED WALL ENCLOSURE STRUCTURES

Abstract: *The article provides an experimental analysis of the behavior and changes in thermophysical properties of the thermal insulation systems most commonly used in construction during the entire life of the buildings. Experimental data on temperature fluctuations and distribution of heat flow density of a thermally modernized section of a wall-enclosing structure insulated by various methods for 6 years were obtained and the values of the actual coefficients of thermal conductivity of various heat-insulating materials were compared in the first approximation. The need to assess the influence of the service life on the thermophysical properties of heat-insulating materials used in the thermal modernization of buildings of various purposes is experimentally substantiated.*

Keywords: *energy efficiency, thermomodernization, thermal insulation, heat transfer, heat flow.*

Introduction

At the current stage of the development of technical solutions aimed at increasing the efficiency of the use of energy carriers, the main factor of energy saving in buildings is the degree of thermal energy saving. One of the instruments of influence on the reduction of energy dependence of the state is the introduction of energy efficiency requirements into the legislative framework. The modern direction of Ukraine's development dictates the need to adapt the current legislative and regulatory framework to the European one, as well as the need to develop new standards in the field of energy efficiency of the building stock, including the quality of the microclimate in buildings. The system complex of regulatory documents establishes mandatory requirements for energy safety, standardization of physical indicators characterizing the fulfillment of these requirements, rules for evaluating energy efficiency indicators at the stage of designing construction objects, their experimental manufacture and use when putting buildings into operation, and during their operation, test methods and criteria for evaluating the conformity of construction products and objects according to energy efficiency indicators [1].

In the new edition of DBN V.2.6-31:2021 "Thermal insulation and energy efficiency of buildings", the normative heat transfer resistance of the external walls of residential buildings for the I climate zone is 4 m^2K/W (increase by 20%), and for transparent enclosing structures 0.9 m^2K/W (20% increase) [2].

Table 1 shows the dynamics of changes in normative heat transfer resistances of enclosing structures of residential and public buildings.

Table 1. *Dynamics of changes in normative heat transfer resistance indicators of the enclosing structure of residential and public buildings*

Type of enclosing structure	Normative heat transfer resistance Rq min, m²K/W							
	1981	1993	2006 I zone	2013 II zone	2017		2022	
					I zone	II zone	I zone	II zone
Outside walls	0.95	2.2	2.8	3.3	3.3	2.8	4.0	3.5
Translucent fencing structures	0.48	0.53	0.6	0.75	0.75	0.6	0.90	0.70

At the moment, Ukraine is dynamically moving towards European standards of thermal insulation, which is reflected in the consistent growth of normative heat transfer resistance values for enclosing structures (Fig. 1).

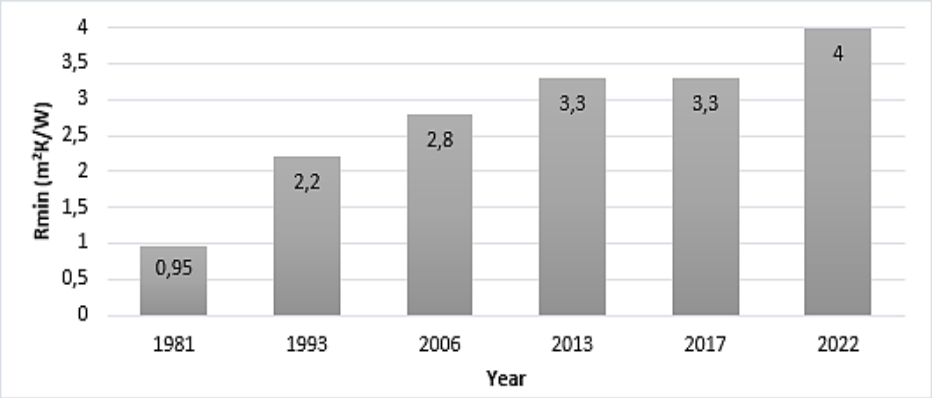

Figure 1. *Dynamics of the development of the coefficient of normative thermal resistance Rn, external walls in the territory of Ukraine*

The main method of bringing the thermal insulation of the enclosing structures of buildings to the standards is the measures of full or partial thermal modernization [1], namely thermal renovation of the enclosing structures, the main measures of which are the replacement of window structures and the installation of an additional layer of thermal insulation on the external walls.

Since thermal renovation measures require significant capital investments, there is a need for a comparative analysis of the heat-technical and economic efficiency of using one or another heat-insulating material. At the same time, it is also important to take into account the durability of coatings under different operating conditions. In this regard, there is a need for multi-variant thermal renovation of individual rooms and experimental studies of their air-temperature regimes and the corresponding amounts of heat loss through the fences of each room.

An innovative project was aimed at solving this problem, the purpose of which was to substantiate ways of reducing the heat consumption of existing administrative buildings by reducing heat loss due to the implementation of optimal options for thermal renovation of enclosing building structures and researching the effectiveness of thermal renovation measures during long-term operation of the structure. The object of the research and the place of application of the project results was the construction of building No. 1 of the Institute of Engineering Thermophysics National Academy of Sciences of Ukraine on Bulakhovsky St., 2 in Kyiv.

The purpose of the study is to analyze the results of experimental studies of heat transfer through heat-insulated wall enclosing structures in real climatic conditions of long-term operation.

Results

Thermal renovation was carried out by replacing the old windows in the premises with modern double-glazed windows and by installing heat-insulating coatings made of different types of materials on part of the area of the outer surface of the fences on the north facade of the building (Fig. 2). In order to exclude the influence of a roof without an attic and a floor without a basement, measures were taken in the premises of the second floor of the investigated building.

By means of a comparative analysis of literature data on the heat-technical characteristics of heat-insulating materials, the following insulation options were selected: basalt wool, foam glass, spraying polyurethane foam, extruded polystyrene foam, PPS-15, PPS-25 and PPS-35 polystyrene foam.

Figure 2. *Scheme of insulation of the enclosing structures of the upper floor of building No. 1 of the Institute of Engineering Thermophysics National Academy of Sciences of Ukraine*

To experimentally determine the dependence on weather conditions of the temperature state of building structures with a layer of insulation, a measuring complex is used, which includes sensors, secondary devices, a convector and a personal computer equipped with special software for further data processing [3].

Quantification of heat loss of wall enclosing structures is determined by installing heat flow converters with a built-in platinum resistance thermometer (PRT) and copper resistance thermometers (CRT), which were used to record temperature indicators. These sensors are installed between the wall and the insulation and on the outer surface of the insulation. They were located practically on one axis, perpendicular to the surface of the wall in such a way as to avoid the influence of sources of heat and moisture release, as well as supply and exhaust openings in the center of a typical thermally homogeneous area (Fig. 3).

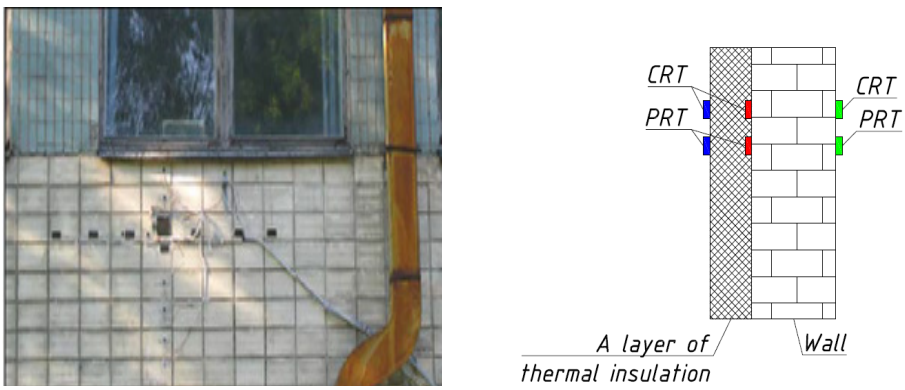

Figure 3. *Installation of resistance thermometers*

The defining thermophysical characteristic of heat-insulating materials is their coefficient of thermal conductivity, which actually determines the reduced resistance of heat transfer through the enclosing structure. To prevent the influence of solar radiation, the most stable experimental data from temperature and heat flow sensors obtained at night are used for calculations.

When calculating heat losses through the enclosing structures of buildings and structures, the value of their heat transfer resistance is usually used:

$$R_{\Sigma} = \frac{1}{\alpha_1} + \sum_{i=1}^{n} \frac{\delta_i}{\lambda_i} + \frac{1}{\alpha_2} \quad (1)$$

where:

α_1 – coefficient of heat transfer from indoor air to the enclosing structure (8.7 W/m²·K);

α_2 – coefficient of heat transfer from the enclosing structure to the outside air (23 W/m²·K);

δ_i – the thickness of the layer of the enclosing structure, m;

λ_i – coefficient of thermal conductivity, W/m·K.

Over the course of five years, a series of experimental studies of heat transfer through a wall-enclosing structure was conducted in the conditions of the real climate of Kyiv, and a large array of experimental data was obtained. Since the system works in the mode of permanent fixation of the values of the heat flow densities through the thermomodernized enclosing structure, the temperatures of the surfaces of the OC layers and the air of the internal and external environment, the analysis of the information obtained in this way for the entire period makes it possible to determine the effectiveness of various heat-insulating materials in terms of reducing heat loss through the fences of the house and improving the temperature regimes of each of the premises. Temperature and heat flux values were recorded and recorded every 10 minutes.

Experimental and calculated values of thermal conductivity coefficients of heat-insulating layers were determined by the average values of all necessary parameters. A comparative analysis of the actual coefficients of thermal conductivity, calculated based on the data of 2013 and 2019, is shown in the diagram of Figure 4.

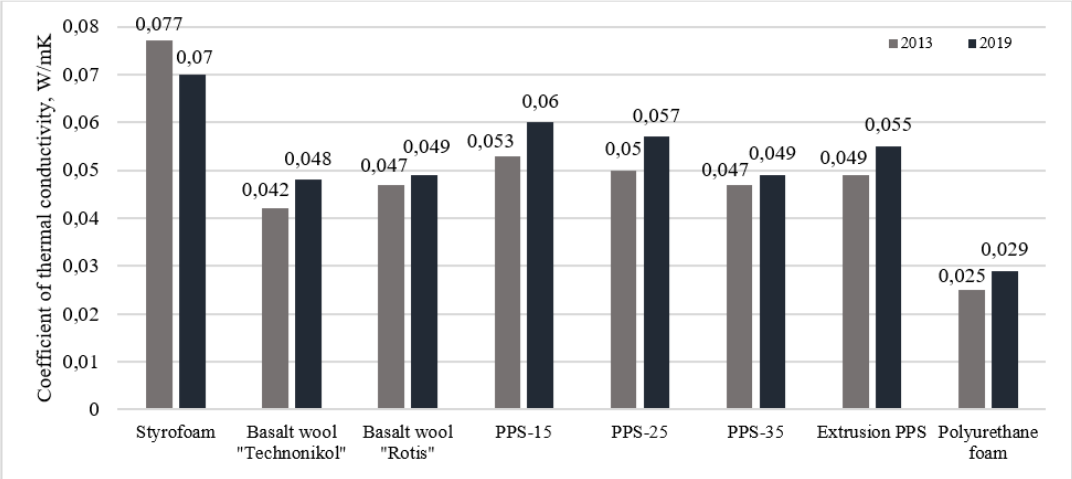

Figure 4. *Experimental and calculated resistances of heat transfer of the enclosing structure for various insulation options*

The graphs in Figure 4 show that the coefficient of thermal conductivity increases during operation. In the future, this factor should be taken into account when conducting engineering calculations. At the same time, the value of thermal conductivity of heat-insulating materials depends on the density of the material, temperature and humidity.

Based on the calculated values of thermal conductivity coefficients of thermal insulation layers according to formula (1), the heat transfer resistance of the entire enclosing structure was calculated for each layer of insulation (Fig. 5).

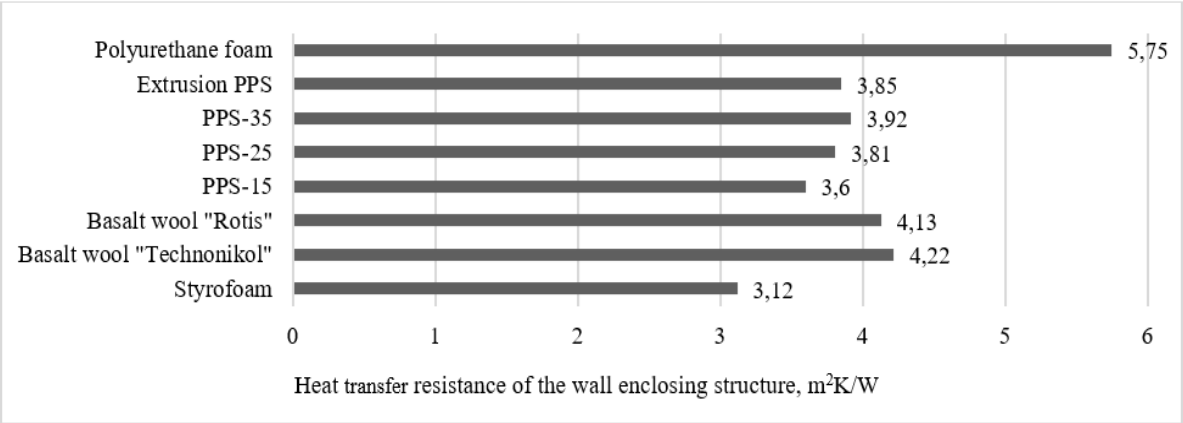

Figure 5. *Experimental and calculated resistances of heat transfer of the enclosing structure for various insulation options*

The main factors of energy efficiency there are the quality of thermal protection of protective structures, ensuring the requirements of thermal comfort of premises, the use of energy-saving systems, technologies and measures. According to the results of impact studies he used of heat-insulating materials in buildings can be claimed to be highly effective in reducing heat loss, buildings through protective structures.

Conclusions

From the results of experimental studies, it follows that an additional layer of insulation on the outer surface of the supporting wall structure contributes both to an increase in the temperature of this surface and to a decrease in the range of its fluctuations with a significant change in the ambient temperature. During long-term operation, heat-insulating materials are constantly exposed to seasonal temperature cyclical effects, and are in a somewhat moistened state, which leads to deterioration of the thermophysical characteristics of the materials.

The need to assess the influence of the service life on the thermophysical properties of heat-insulating materials used in the thermal modernization of buildings of various purposes is experimentally substantiated.

Also, the given results show that the thermal conductivity coefficient increases during operation and should be taken into account during engineering calculations in the future.

The use of experimental and theoretical studies makes it possible to obtain comprehensive information about the thermal properties of enclosing structures and their influence on the energy efficiency of buildings. An important, little-studied factor in the choice of thermal insulation and the design of the building's thermal envelope is the change in the thermal physical characteristics of thermal insulation materials during long-term operation during the service life of the building itself.

The article was written with the assistance of the National Research Foundation of Ukraine within the framework of project No. 208/0172 “Aerodynamics, heat exchange and innovations for increasing the energy efficiency of window structures and their use for the reconstruction of war-damaged buildings in Ukraine”.

References

[1] DSTU-N B V.3.2-3:2014. Guidelines for thermal modernization of residential buildings. Effective from 12/31/2014. Kyiv: Minregion of Ukraine. 67 p.

[2] DBN V.2.6-31:2021. Thermal insulation and energy efficiency of buildings. K.: Minregion of Ukraine, 2022. 23 p.

[3] Basok, B.I., Davydenko, B.V., Honcharuk, S.M. (2013). *Various thermal renovation of the enclosing structures of part of the floor of the existing administrative building and monitoring of heat losses during its long-term operation*. Science and Innovation, Vol. 9, No. 2, pp. 18–21.

Andrii CHEILYTKO, Oguzhan NOHUTCU
Peter SCHWARZBÖZL, Robin Tim BROESKE
German Aerospace Center (DLR), Institute of Solar Research, Karl-Heinz-Beckurts-Straße 6, 52428 Juelich, Germany
Corresponding author: andrii.cheilytko@dlr.de

Doi: 10.53412/jntes-2023-3-2

CFD SIMULATION OF AIRFLOW IN A NEW RECEIVER CONCEPT FOR SOLAR TOWER

Abstract: *Open cavity solar receivers play an important role in concentrated solar power (CSP) systems and hold great promise, particularly in scenarios where their ability to absorb high fluxes at very high temperatures yields beneficial results. This intense concentration of sunlight can be used to produce electricity through various means, such as generating steam to drive a turbine. The efficiency of the open volumetric receiver concept relies heavily on the air return ratio (ARR) which refers to the proportion of air recirculated and returned to the receiver. A high ARR contributes to high receiver efficiencies, as with rising ARR, the reused part of the enthalpy of warm air increases. This paper deals with the design and simulation of a new receiver concept with a conical cavity and square cross-section. The objective is to identify the most effective design arrangement for the square-cone structure, considering different depths, that maximizes both the air return ratio (ARR) and thermal efficiency. The findings demonstrate that increasing the depth of the mentioned receiver leads to a rise in the ARR, up to a certain threshold which can reach values up to 94.53%, beyond which there is a subsequent decline in efficiency. Furthermore, this study examined how varying the amount of air passing through a specific section of the receiver across a defined area, along with the temperature changes in these sections, affected its operational efficiency.*

Keywords: *solar tower, cavity receiver, air return ratio, convective efficiency, CFD simulation, airflow analysis.*

Introduction

CSP offers the benefit of storing generated energy and providing a continuous supply when needed. Its high energy efficiency makes it a competitive alternative to coal and nuclear power plants [1]. These aspects make this technology an attractive option for meeting future energy needs. One type of CSP is solar towers, which use different kinds of solar receivers to convert solar radiation into thermal energy.

Open volumetric receiver (OVR) technology stands out as an interesting advancement in concentrated solar power (CSP) because of the high temperatures that can be reached by the heat transfer fluid (air at ambient pressure), leading to a highly efficient power cycle. The design of OVRs allows the receiver to interact with the surrounding atmosphere and adjust the amount of air accordingly. Depending on the particular application and limitations, their shapes and arrangements may differ, commonly taking on cylindrical or rectangular forms with suitable openings or connections for air intake and outlet [2].

Figure 1 depicts the basic layout of the cavity receiver, which has a modular receiver concept. Each receiver module was constructed as an open cavity with an inner square cone shape. In the illustrated model, air entered the cavity through the inlet absorber, which was first heated to 450°C. Once inside the cavity, air is sucked through the main absorber, where it reaches its eventual temperature of 700°C.

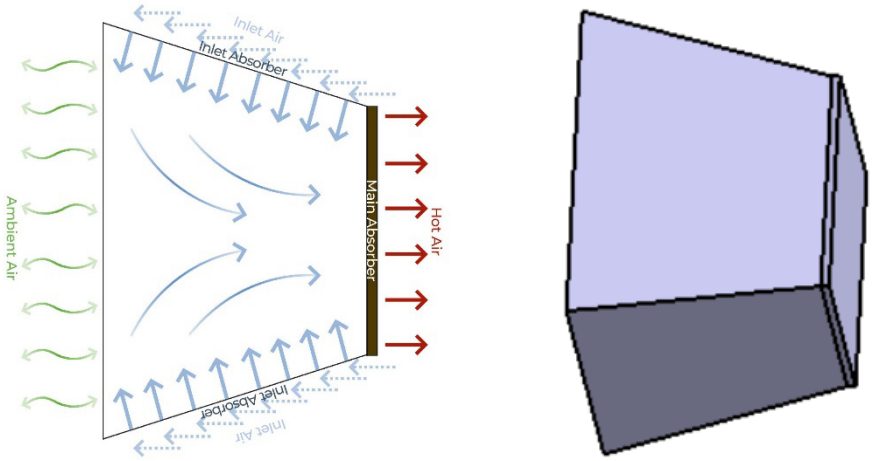

Figure 1. *Illustration of the new concept of cavity receiver for solar tower*

To understand the ARR of a cavity receiver, it is important to point out this parameter. The ARR represents the fraction of the inlet air redirected back into the main absorber (Equation 1).

$$\mathrm{ARR} = \frac{\dot{m}_{\mathrm{ReturnedInletAir}}}{\dot{m}_{\mathrm{HotAir}}} \tag{1}$$

A high ARR contributes to high receiver efficiencies because with rising ARR values, the reused part of the enthalpy of warm air increases. The ARR is of vital importance in maximizing receiver efficiency, especially when high return air temperatures are advantageous for subsequent processes [3].

Calculations of the air return ratio were conducted using ANSYS (Version 2023 R1). The ARR computations were conducted for four distinct setups, ranging from 50 mm to 200 mm, with intervals of 50 mm. The results demonstrate that the optimum ARR was achieved with an aperture depth of 150 mm.

Method and Model

For simplicity of explanation, the upcoming analyses will focus on the inner section of the cavity receiver. The computational fluid dynamics (CFD) software ANSYS CFX (Version 2023 R1) was employed to perform computations to determine the best variation for receiver configurations with varying aperture depths.

For the first part of the analysis, simulations were performed to determine the ARR, ultimately revealing which aperture depth provides the highest level of efficiency. In the depicted model, air at 450°C enters the cavity through the inlet absorber at a mass flow rate of 0.07 kg/s. Inside the cavity, the air undergoes a heating process until it reaches an eventual temperature of approximately 700°C.

In the second part of the model analysis both mass flow and temperature gradients will be introduced to the inlet of the receiver to investigate the influence of this parameters on the ARR.

Geometry. To determine the ideal design of the absorber, both simulation approaches were examined under different depth variations from 50 mm to 200 mm at intervals of 50 mm. All absorber designs have an aperture length of 200 mm, whereas the length of the top side was defined as 140 mm. The main absorber is a wire mesh absorber with a 5 mm thickness and has a porous structure, as shown in Figure 2. The main absorber in the designed model utilizes a volume porosity of 0.5.

The porosity of a material is a measure of its void space. The higher the porosity, the greater the void space in the material. As for the described model a porosity factor of 0.5 was applied. A porous surface enhances heat transfer and reduces thermal losses by increasing the surface area available for absorbing and transferring heat from the incoming air or heat transfer medium [4].

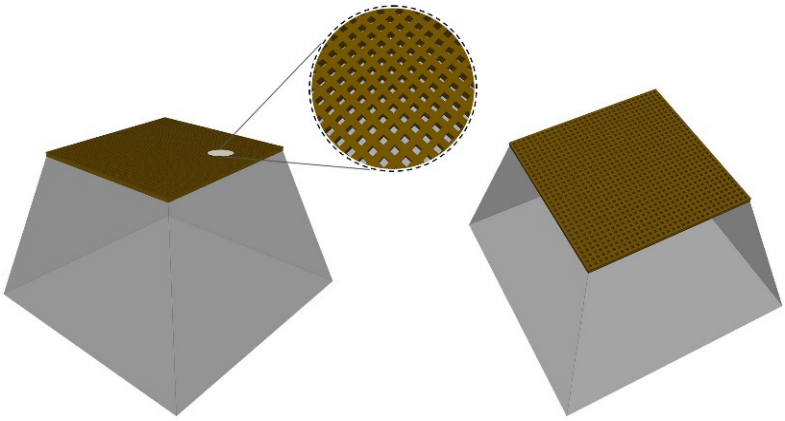

Figure 2. *Porous main absorber in new concept of receiver for solar tower (wire mesh region for inlet absorber not shown)*

Mesh Method. The examination of the square-cone shaped receiver covers two distinct points: determination of the optimal design for the receiver and subsequently analysis of the effect of both a mass flow gradient and temperature gradient to assess their respective influences on the ARR.

The computational grids employed for the model are composed of structured meshes, generated using ANSYS. Structured meshes comprise orderly grids featuring a consistent layout, making them suitable for relatively uncomplicated and uniform shapes. When dealing with geometries that align effectively with these grids, this mesh type can result in a more accurate portrayal of flow and heat transfer phenomena [5].

To determine the optimal geometry, a methodology referred to as "approach one" was employed. To represent the airflow between the opening of the receiver and surrounding a computational space for the ambient was added to the model. The computational space for the ambient has a domain length of five times the receiver's dimension along the direction of the flow, with a width twice that of the receiver to provide enough space for the flow to adjust to the presence of the geometry as suggested by Cagnoli et al. [6].

As evident in the Figure 3, the mesh becomes more refined towards the edges of the receiver. This refinement enhances the resolution, enabling a more detailed analysis of buoyancy effects and boundary conditions.

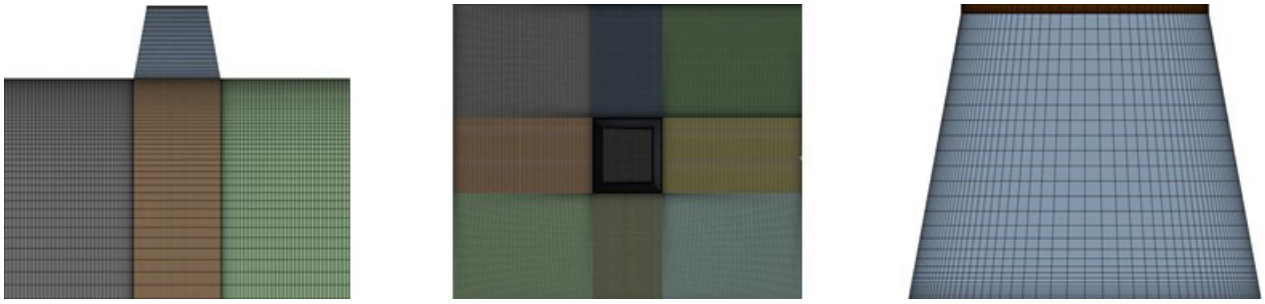

(a) Front View (b) Top View (c) Receiver

Figure 3. *Meshing for approach one*

For the second approach, shown in Figure 4, the absorber configuration is divided into five distinct segments. This segmentation allows for the integration of varying mass flow and temperature gradients, ultimately contributing to the calculation of their respective ARR values at a later stage. To further enhance the precision of the outcomes, the mesh was configured to be more refined at the interfaces between these sections and denser towards the edges. This approach mirrors the technique previously employed in approach one, ensuring a thorough and accurate analysis.

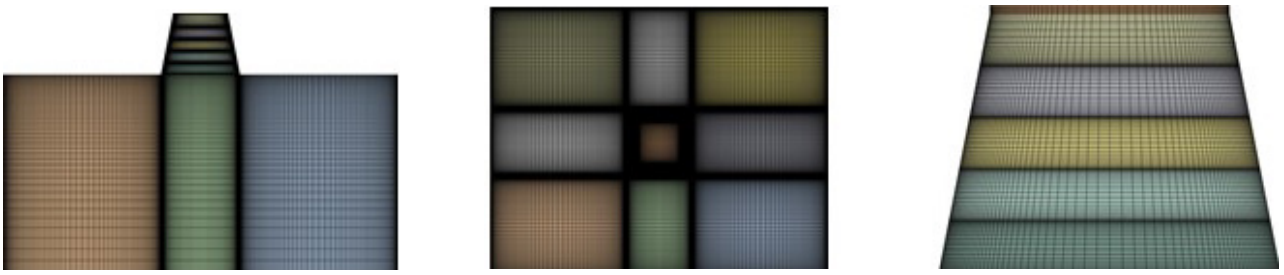

(a) Front View (b) Top View (c) Receiver

Figure 4. *Meshing for approach two*

Simulation Strategy. Having a good configuration for the simulation setup of the CFD model is an essential task, and particular attention is paid to these conditions due to their critical role in achieving precise solutions for fluid flow and heat transfer calculations.

The examination will employ the pressure-based methodology, as it deals with low-speed, incompressible airflow for the receiver. The model incorporates two distinct phases of air, each treated as an ideal gas, one for the incoming air and another for the ambient, indicating the utilization of multiphase simulations.

It is important to select a reasonable turbulence model that aligns with the constructed model. Given these considerations, the *k*-omega-SST turbulence model emerges as the most appropriate choice. This model aligns well with the structured meshes employed for the receiver, particularly in scenarios when dealing with complex flows [7].

Theory and Calculation

Efficiency calculations were conducted to assess the effectiveness of the receiver variations. An efficiency of 1, or 100%, if expressed as a percentage, indicates a perfectly efficient system in which all inputs are converted into useful outputs. In real-world scenarios, this is rarely achieved, owing to the manifold losses experienced by the receiver. In the context of this paper the convective efficiencies of the respective receivers will be derived.

Various approaches can be used to compute the convective efficiency of the system. Here, the efficiency ratios are calculated using the return efficiency methodology outlined by Cheilytko A. et al. [8]:

$$Q_{\text{full}} = Q_{\text{useful}} + Q_{\text{loss}} \tag{2}$$

$$1 = \eta_{conv} + \frac{Q_{\text{loss}}}{Q_{\text{full}}} \tag{3}$$

$$\eta_{conv} = 1 - q_{\text{loss}}^{\text{air}} \tag{4}$$

Equation (2) to Equation (4) outlines the derivation of the return efficiency method, where the convective heat loss is subtracted from 1. This resultant value is then interpreted as the convective heat efficiency of the receiver. Equation (5) can be used to compute $q_{\text{loss}}^{\text{air}}$ once the necessary values $Q_{\text{loss}}^{\text{air}}$ and I_{rec} are acquired for the system:

$$q_{\text{loss}}^{\text{air}} = \frac{Q_{\text{loss}}^{\text{air}}}{I_{\text{rec}}} \tag{5}$$

$Q_{\text{loss}}^{\text{air}}$ represents the energy loss owing to the heat from the air leaving the solar plant to the environment. To derive $Q_{\text{loss}}^{\text{air}}$ (Eq. 6) for the calculation of $q_{\text{loss}}^{\text{air}}$ the obtained ARR values (Table 1) for varying receiver depths were used. Additionally, the enthalpy values for the ambient and inlet air are obtained from the heat atlas [9]. The enthalpy values are primarily dependent on the temperature of the

air as an ideal gas, which is 22°C for the ambient temperature and 450°C for the inlet. At these respective states the enthalpies are respectively -3.01 kJ/kg and 440.330 kJ/kg. ε is a delay factor related to the time required to heat the exhaust air to a given temperature, which will be taken 1 for the upcoming calculations since we are dealing with stationary case [10].

$$Q_{loss}^{air} = \left(H_{out}^{air} - H_{amb}^{air}\right) \cdot \left(1 - ARR\right) \cdot \varepsilon \tag{6}$$

where:

H_{out}^{air} – enthalpy carried by air (kJ/s);

H_{amb}^{air} – enthalpy brought in with ambient air (kJ/s);

ε – delay factor.

I_{rec} is the power received from sunlight on the surface of the receiver, determined by both the aperture area of the receiver and the incident solar radiation. The previously computed incoming solar radiation directed at the receiver was established in Solar Tower Juelich (STJ).

In ANSYS CFX environment, the corresponding ARR values were calculated for different receiver depths, as listed in the table below.

Table 1. *ARR values obtained for different geometry variations*

h **[mm]**	***ARR*** **[%]**
50	87.66
100	92.90
150	94.53
200	94.24

Upon calculating the total loss by integrating the derived values into the respective equations, the corresponding convective efficiency values for the geometric alterations are listed below.

Table 2. *Convective heat efficiency distribution for different geometry variations*

h **[mm]**	***η*** **[%]**
50	88.03
100	93.11
150	94.69
200	93.44

Comparing these two tables, it can be concluded that the convective heat efficiency is proportional to ARR.

Results

Analysis on the Receiver Geometry. The assessments provided in this section rely on CFD simulations conducted using ANSYS CFX. The data under examination were obtained from steady-state RANS calculations. Post-processing of the effects and results was conducted and analyzed using the CFX post. These effects are visualized in the model developed by contour plots and gradients of various flow quantities contained in the output dataset. This allowed for the visualization and examination of the air entering the receiver and exiting the main absorber. The optimal variation is emphasized by evaluating diverse geometric alterations. This will allow conclusions to be drawn about the effects of geometry adaptations and the consequences of the mass flow and temperature gradients.

Thermal Analysis. The thermal efficiency analysis was performed by analyzing the contour plots shown in Figure 5. Because the receiver contains an aperture, a portion of the exhausted air is naturally lost to the ambient air and substituted with the surrounding air as a consequence of the buoyancy effect.

Buoyancy effects can have a significant impact on the efficiency of cavity-air receivers. Contour plots of the total inlet air temperature were used to analyze these effects. During the heating process, the receiver becomes less dense and rises owing to the buoyancy. This creates a natural flow circulation resulting from the cooler air entering the bottom and warmer air rising to the top [11]. This circulation helps to distribute heat more evenly within the receiver, which can improve the overall efficiency. It is evident from Figure 5 that the best heat distribution was achieved at a depth of 150 mm. The heat was almost evenly distributed over the walls of the receiver, contributing to the maintenance of a more stable and efficient operation. For other variations, some localized overheating can be observed, which can lead to potential structural damage. By maintaining more uniform temperatures, buoyant flow can help reduce thermal stress on the receiver material, which can lead to a longer lifespan of the receiver and improve its overall reliability.

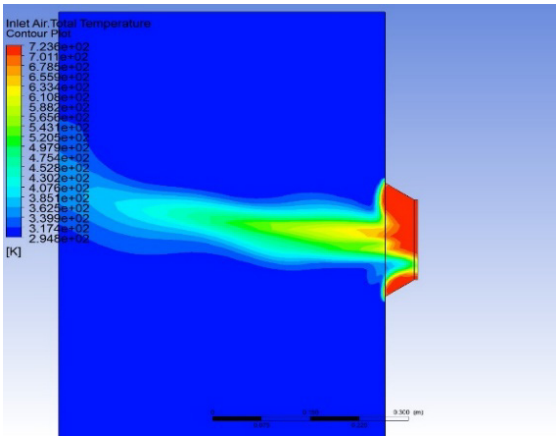

(a) Inlet total temperature contour for 50 mm depth

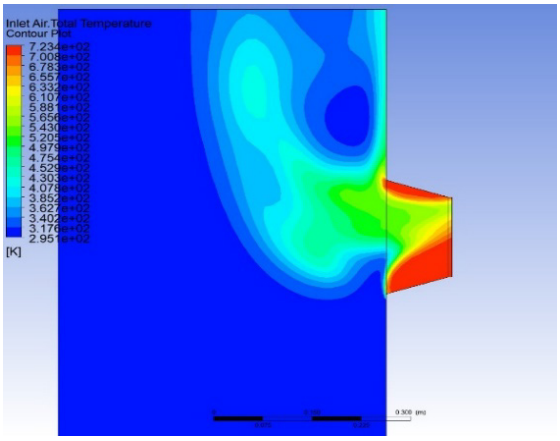

(b) Inlet total temperature contour for 100 mm depth

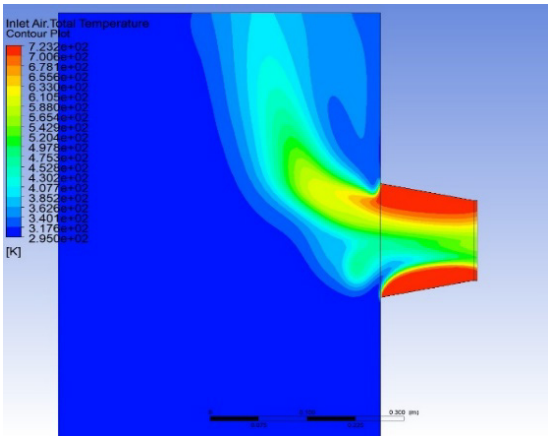

(c) Inlet total temperature contour for 150 mm depth

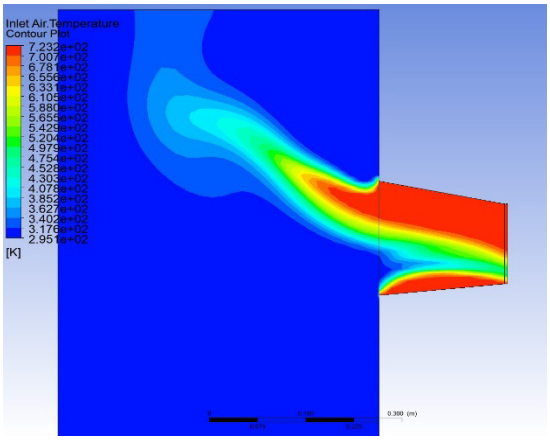

(d) Inlet total temperature contour for 200 mm depth

Figure 5. *Comparison of the inlet total temperature contour plots for the different geometry variations*

Analysis of the Effect of the Receiver Depth on the ARR. An examination will be conducted focusing on the ARR with respect to receiver depths of different variations. The analysis was facilitated by the generation of contour plots representing the inlet air velocity. This visualization technique offers a deeper understanding of how varying receiver depths affect ARR. The figures above show the partial loss of warm air from the environment. As losses increase, ARR decreases, and thus, efficiency decreases.

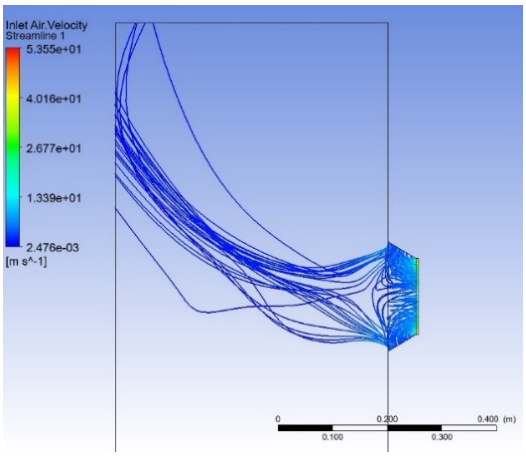

(a) Partial loss of warm air to the ambient for 50 mm depth

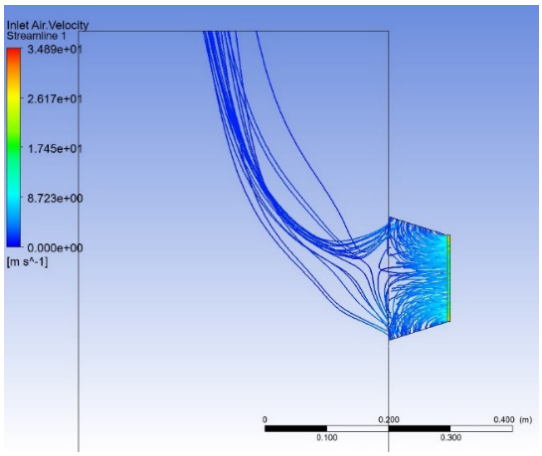

(b) Partial loss of warm air to the ambient for 100 mm depth

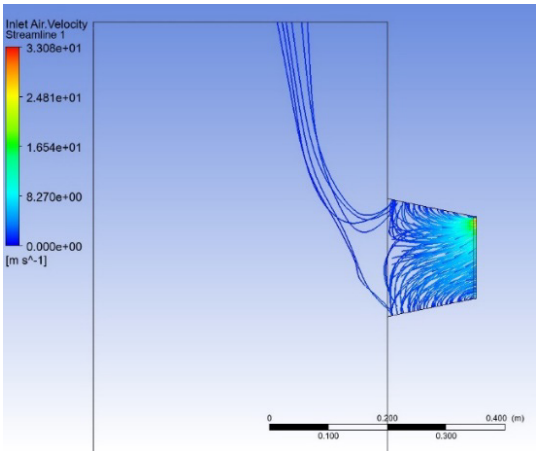

(c) Partial loss of warm air to the ambient for 150 mm depth

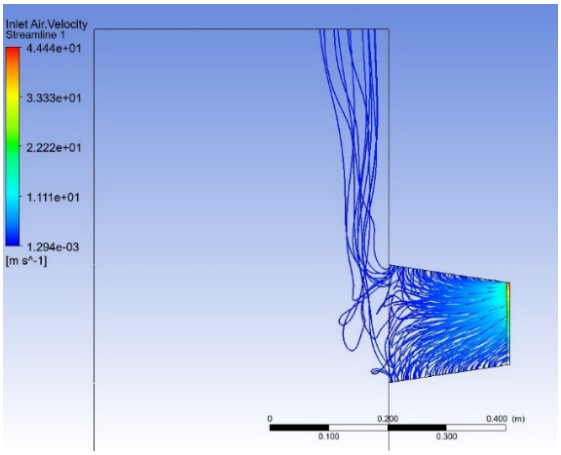

(d) Partial loss of warm air to the ambient for 200 mm depth

Figure 6. *Comparison of the partial loss of warm air to the ambient for different geometry variations*

An examination will be conducted focusing on the ARR with respect to receiver depths of different variations. The analysis was facilitated by the generation of contour plots representing the inlet air velocity. This visualization technique offers a deeper understanding of how varying receiver depths affect ARR. The figures above show the partial loss of warm air from the environment. As losses increase, ARR decreases, and thus, efficiency decreases.

It should be noted that the heat dissipation to the ambient decreases steadily up to a receiver depth increase of 150 mm, but then starts to increase again. These contour plots validate the accuracy of the earlier calculations for the ARR. This indicates a critical point at a depth of 150 mm, beyond which the heat loss begins to increase.

Moreover, the flow dynamics within the receiver play a major role. As air flows into the receiver, it encounters resistance that is directly proportional to velocity leading to a pressure drop. The pressure subsequently leads to a decrease in the overall efficiency. As the velocity increases, the pressure drop also increases, but not necessarily in a linear fashion. As can be seen in the sub-figures, it is evident that the lowest inlet air velocities are obtained with 150 mm resulting in the lowest loss also the flow of the air is smooth and orderly.

The flow regime within the receiver is crucial. When velocities are low, the flow tends to be smooth and orderly, leading to a laminar pattern. However, at higher velocities, it can shift into irregular patterns, as demonstrated for the 200 mm receiver depth. Beyond a receiver depth of 150 mm, there is an increase in the inlet air velocity, resulting in a higher pressure drop, and the flow adopts an irregular pattern, consequently leading to a decrease in efficiency and subsequently reducing the ARR.

Analysis of the Gradient of Mass Flow and Temperature along the Receiver. A clarification for the impact of both the mass flow gradient and the temperature gradient along the receiver surface will be made. These gradients will be incorporated into the receiver through two distinct approaches. In the initial scenario, there will be an increase to the main absorber, while in the subsequent case, an increase will be made to the aperture.

The examination of these gradients provides valuable insights into how variations in mass flow and temperature can influence the overall performance of the receiver system. By specifically targeting the main absorber and aperture, the aim to gain a comprehensive understanding of the interaction between these factors and their effects on the system's efficiency limits. This investigation is important in optimizing the design and operation of the receiver for enhanced performance. As the maximum efficiency has been obtained for a receiver depth of 150 mm, the following analyses will be based on this variation.

Mass Flow Gradient. The open cavity receiver is partitioned into five segments of uniform height. This division serves to implement the mass flow gradients for CFD simulations under different mass flow loads.

In the analysis of mass flow gradients, adjustments will be applied in two distinct orientations: one towards the main absorber and the other to the aperture as shown in Figure 7. Furthermore, the mass flow gradients will be introduced at three varying levels, specifically 25% and 50% respectively for full load (0.0700 kg/s), 75% load (0.0525 kg/s), and 50% (0.0350 kg/s) load.

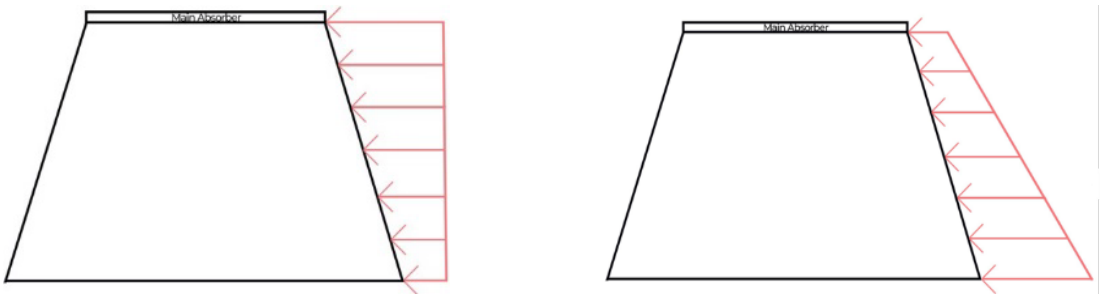

(a) Gradients Increasing to the main absorber (b) Gradients Increasing to the aperture

Figure 7. *Ilustration of the orientation of the relative mass flow gradients along the receiver*

To enhance comprehension, Figure 8 assigns numerical labels to the segments utilized for the introduction of the mass flow gradients. Corresponding values indicating the variation in mass flow for the mentioned scenarios are provided in Tables 3–8.

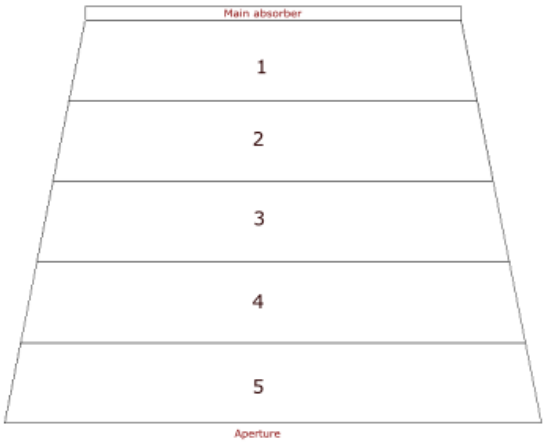

Figure 8. *Number labeling of the segments*

To illustrate the influence of the mass flow gradient, an observation centered around the utilization of a 150 mm receiver depth is presented, as it has demonstrated the highest ARR. The mass flow for each segment are calculated as shown in Equation (7) for different loads:

$$\dot{m}_{segment} = \frac{Area_{segment}}{Area_{total}} \cdot \dot{m}_{load} \tag{7}$$

Table 3. *Mass flow density distribution for full load*

Section	Uniform Mass Flow Density [kg/s·mm²]	50% gradient on Mass Flow Density to aperture [kg/s·mm²]	50% gradient on Mass Flow Density to the main absorber [kg/s·mm²]	25% gradient on Mass Flow Density to aperture [kg/s·mm²]	25% gradient on Mass Flow Density to the main absorber [kg/s·mm²]
1	6.729E-07	3.364E-07	9.053E-07	5.047E-07	7.912E-07
2	6.729E-07	5.047E-07	8.411E-07	6.056E-07	6.729E-07
3	6.729E-07	6.729E-07	6.729E-07	6.729E-07	6.729E-07
4	6.729E-07	8.411E-07	5.047E-07	6.729E-07	6.056E-07
5	6.729E-07	9.053E-07	3.364E-07	7.912E-07	5.047E-07

Table 4. *Mass flow distribution for full load*

Section	Uniform Mass Flow [kg/s]	50% gradient on Mass Flow to aperture [kg/s]	50% gradient on Mass Flow to the main absorber [kg/s]	25% gradient on Mass Flow to aperture [kg/s]	25% gradient on Mass Flow to the main absorber [kg/s]
1	0.0120	0.0060	0.0214	0.0090	0.0187
2	0.0130	0.0097	0.0187	0.0117	0.0164
3	0.0140	0.0140	0.0140	0.0140	0.0140
4	0.0149	0.0187	0.0097	0.0164	0.0117
5	0.0159	0.0214	0.0060	0.0187	0.0090
Total Mass Flow	0.0700	0.0700	0.0700	0.0700	0.0700

Table 5. *Mass flow density distribution for 75% load*

Section	Uniform Mass Flow Density [kg/s·mm²]	50% gradient on Mass Flow Density to aperture [kg/s·mm²]	50% gradient on Mass Flow Density to the main absorber [kg/s·mm²]	25% gradient on Mass Flow Density to aperture [kg/s·mm²]	25% gradient on Mass Flow Density to the main absorber [kg/s·mm²]
1	5.047E-07	2.523E-07	6.790E-07	3.785E-07	5.551E-07
2	5.047E-07	3.785E-07	6.308E-07	4.54E-07	5.551E-07
3	5.047E-07	5.047E-07	5.047E-07	5.047E-07	5.047E-07
4	5.047E-07	6.308E-07	3.785E-07	5.551E-07	4.542E-07
5	5.047E-07	6.790E-07	2.523E-07	5.551E-07	3.785E-07

Table 6. *Mass flow distribution for 75% load*

Section	Uniform Mass Flow [kg/s]	50% gradient on Mass Flow to aperture [kg/s]	50% gradient on Mass Flow to the main absorber [kg/s]	25% gradient on Mass Flow to aperture [kg/s]	25% gradient on Mass Flow to the main absorber [kg/s]
1	0.0090	0.0045	0.0161	0.0067	0.0140
2	0.0097	0.0077	0.0140	0.0087	0.0123
3	0.0105	0.0105	0.0105	0.0105	0.0105
4	0.0112	0.0140	0.0077	0.0123	0.0087
5	0.0119	0.0161	0.0045	0.0140	0.0067
Total Mass Flow	0.0525	0.0525	0.0525	0.0525	0.0525

Table 7. *Mass flow density distribution for 50% load*

Section	Uniform Mass Flow Density [kg/s·mm²]	50% gradient on Mass Flow Density to aperture [kg/s·mm²]	50% gradient on Mass Flow Density to the main absorber [kg/s·mm²]	25% gradient on Mass Flow Density to aperture [kg/s·mm²]	25% gradient on Mass Flow Density to the main absorber [kg/s·mm²]
1	3.364E-07	1.682E-07	4.526E-07	2.523E-07	3.956E-07
2	3.364E-07	2.523E-07	4.205E-07	3.028E-07	3.701E-07
3	3.364E-07	3.364E-07	3.364E-07	3.364E-07	3.364E-07
4	3.364E-07	4.205E-07	2.523E-07	3.701E-07	3.028E-07
5	3.364E-07	4.526E-07	1.682E-07	3.956E-07	2.523E-07

Table 8. *Mass flow distribution for 50% load*

Section	Uniform Mass Flow [kg/s]	50% gradient on Mass Flow to aperture [kg/s]	50% gradient on Mass Flow to the main absorber [kg/s]	25% gradient on Mass Flow to aperture [kg/s]	25% gradient on Mass Flow to the main absorber [kg/s]
1	0.0060	0.0030	0.0107	0.0045	0.0093
2	0.0065	0.0048	0.0093	0.0058	0.0082
3	0.0070	0.0070	0.0070	0.0070	0.0070
4	0.0074	0.0093	0.0048	0.0082	0.0058
5	0.0079	0.0107	0.0030	0.0093	0.0045
Total Mass Flow	0.0350	0.0350	0.0350	0.0350	0.0350

The variation of the ARR with regards to the mass flow gradient, whether introduced to the main absorber (see positive values) or applied inversely to the aperture (see negative values) is represented in Figure 9.

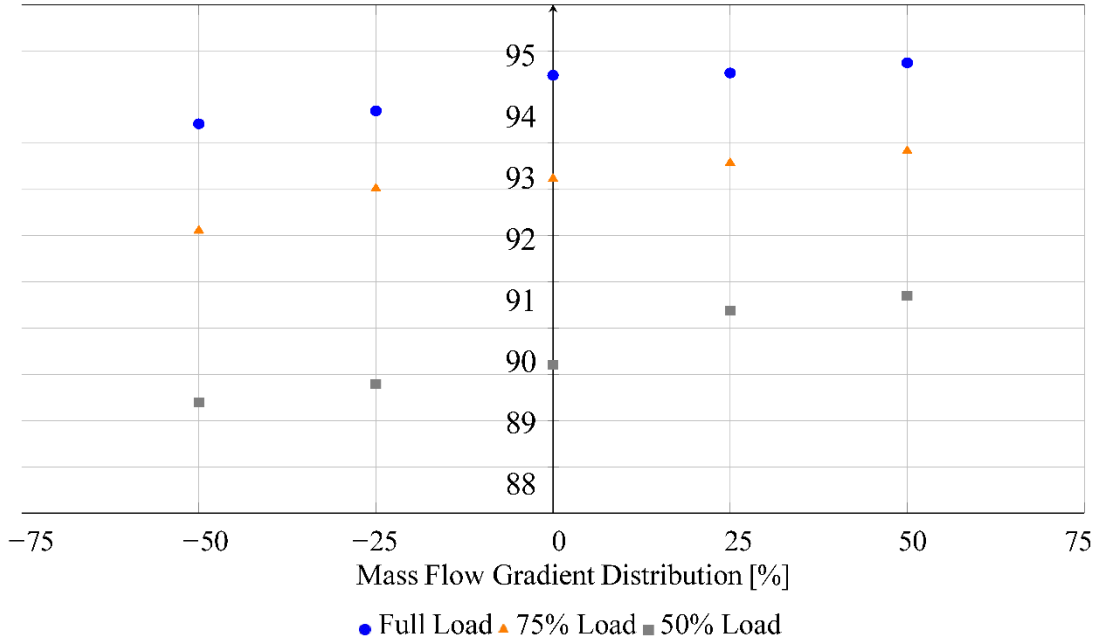

Figure 9. *ARR dependence on the mass flow gradient*

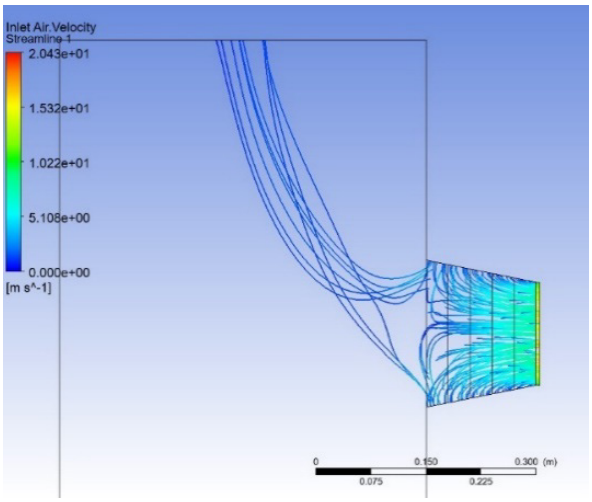

(a) Partial loss of warm air
for 50% mass flow gradient to the main absorber

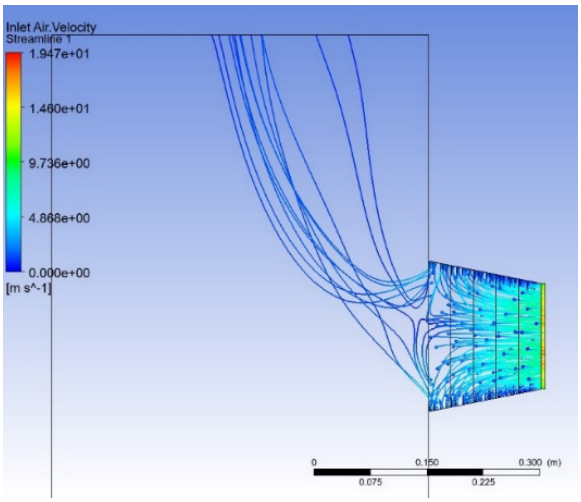

(b) Partial loss of warm air
for 50% mass flow gradient to aperture

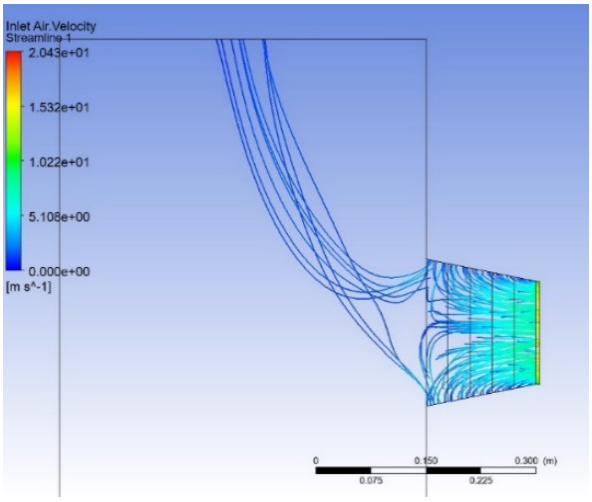

(c) Partial loss of warm air
for 25% mass flow gradient to the main absorber

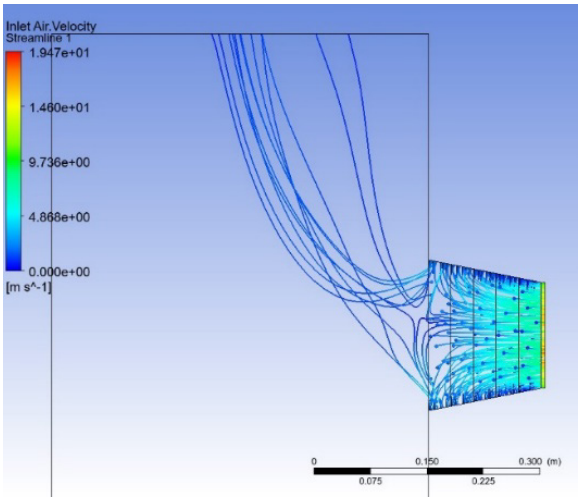

(d) Partial loss of warm air
for 25% mass flow gradient to aperture

Figure 10. *Comparison of the partial loss of warm air to the ambient for different geometry variations*

Increasing the overall mass flow typically results in an increase of the ARR. Nevertheless, it also brings about reduced air temperatures, consequently leading to distinct operational states for the receiver. Hence, the ARR changes in the depicted cases will be evaluated under the same load variations. While this implies that fine-tuning the mass flow is important for increasing system efficiency, it indicates a direct connection between the orientation of the applied mass flow density along the inlet of the receiver. This underscores the significance of the system design for enhanced performance an examination of the cavity's internal dynamics is imperative. Given the relatively consistent inlet air velocities, the examination of warm air loss to the surroundings becomes important for meaningful comparisons (Fig. 10).

Introducing higher mass flow gradients near to the aperture results in increased warm air losses to the environment, consequently increasing overall losses. Specifically, for a mass flow gradient distribution of 50%, the ARR experiences a reduction of roughly 1.5%, while for a distribution of 25%, it decreases by about 0.85%. This underscores the proportional decrease in ARR with increased mass flow near the aperture, as losses become more evident.

Temperature Gradient. Once more, the same method is applied that is used in the mass flow gradient approach, this time with the integration of the temperature gradients in both directions along the receiver. The utilized temperature gradients are set to be respectively 25°C, 50°C, and 75°C along the receiver for this analysis.

Figure 11 shows the ARR values obtained for different loads. It can be seen that incorporating a temperature gradient, by keeping the inlet mass flow constant, has almost no effect on the ARR distribution for the same load distributions.

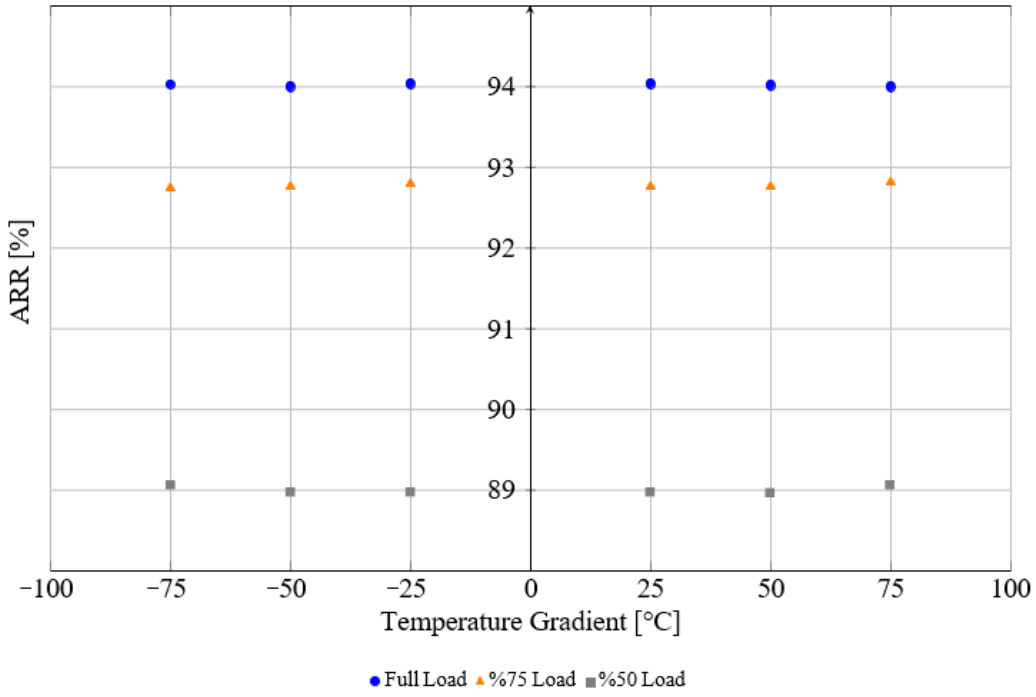

Figure 11. *ARR dependence on the temperature gradient*

The study delves into a comprehensive examination of the interior of the cavity receiver to gain a better understanding. This will involve investigations of both the temperature gradient and the assessment of the losses of the warm air to the ambient.

Furthermore, it is worth noting that the constant dissipation of heat to the ambient is a favorable outcome, as it signifies a stable thermal performance regardless of the applied temperature gradient. The results (Figures 12 and 13) indicate that the implemented temperature gradient influences the temperature distribution in proximity to the walls, but exerts minimal influence on the internal regions of the receiver. Consequently, this has a limited impact on the overall buoyancy forces and overall losses to the environment. Moreover, the heat dissipated to the surroundings remains nearly constant across all scenarios.

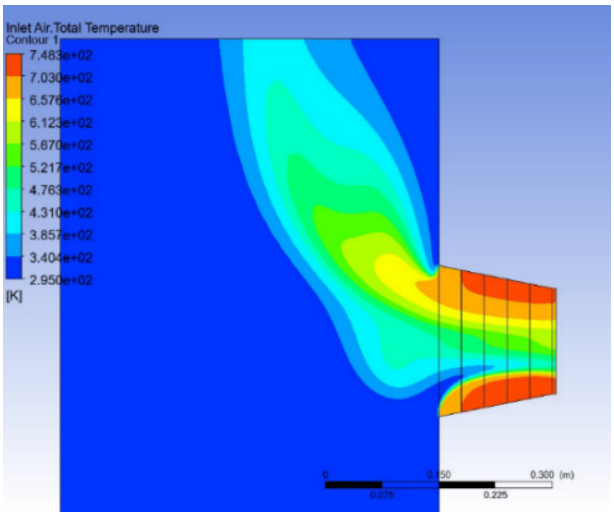

(a) Inlet air total temperature contour
for 25°C temperature gradient to the main absorber

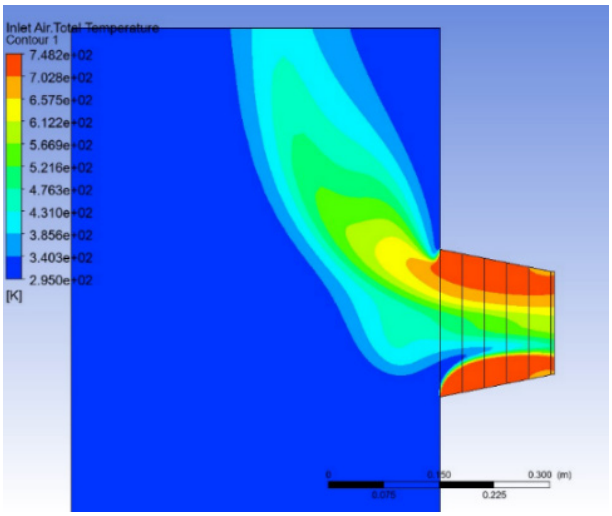

(b) Inlet air total temperature contour
for 25°C temperature gradient to aperture

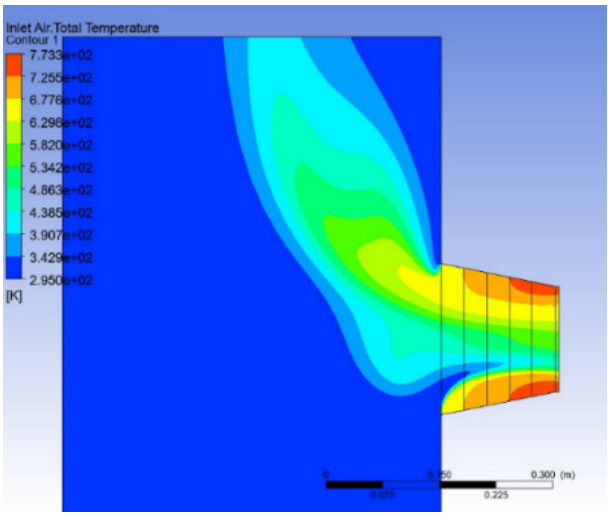

(c) Inlet air total temperature contour
for 50°C temperature gradient to the main absorber

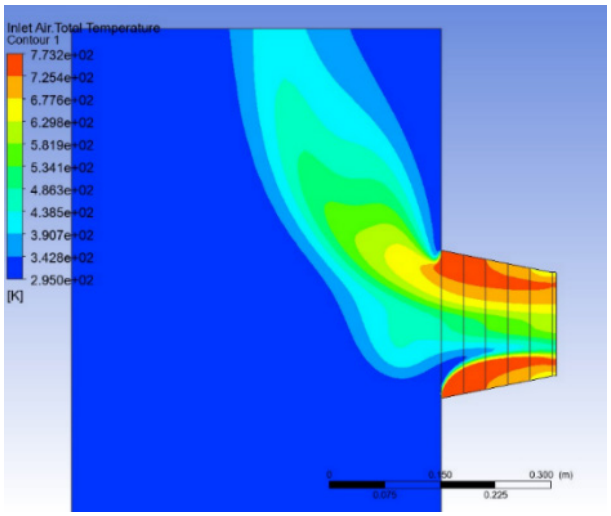

(d) Inlet air total temperature contour
for 50°C temperature gradient to aperture

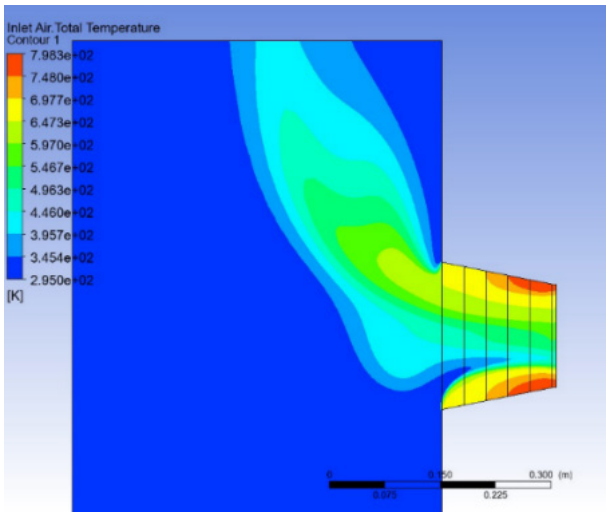

(e) Inlet air total temperature contour
for 75°C temperature gradient to the main absorber

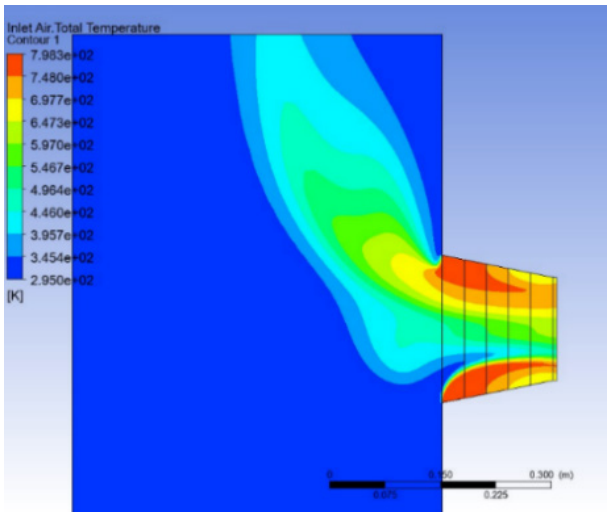

(f) Inlet air total temperature contour
for 75°C temperature gradient to aperture

Figure 12. *Comparison of the inlet air total temperature contour plots for different temperature gradients*

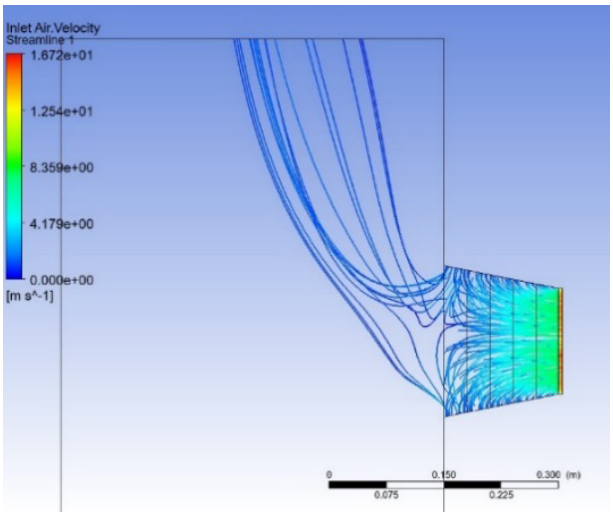

(a) Inlet air velocity contour
for 25°C temperature gradient to the main absorber

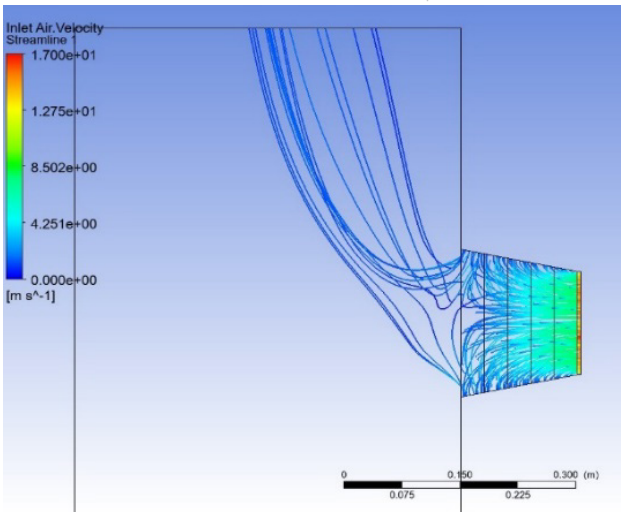

(b) Inlet air velocity contour
for 25°C temperature gradient to aperture

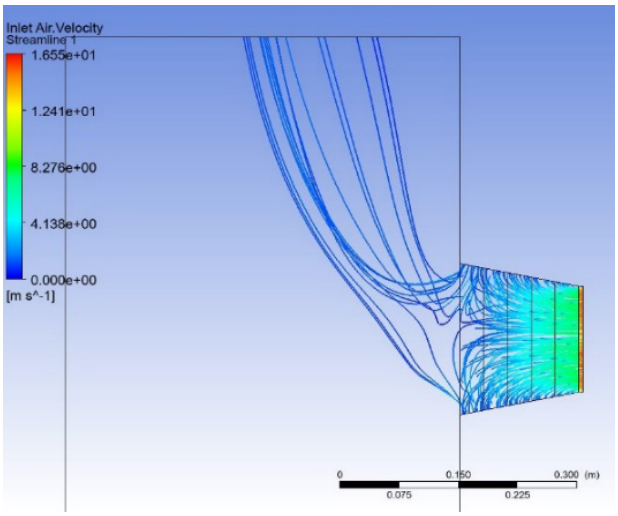

(c) Inlet air velocity contour
for 50°C temperature gradient to the main absorber

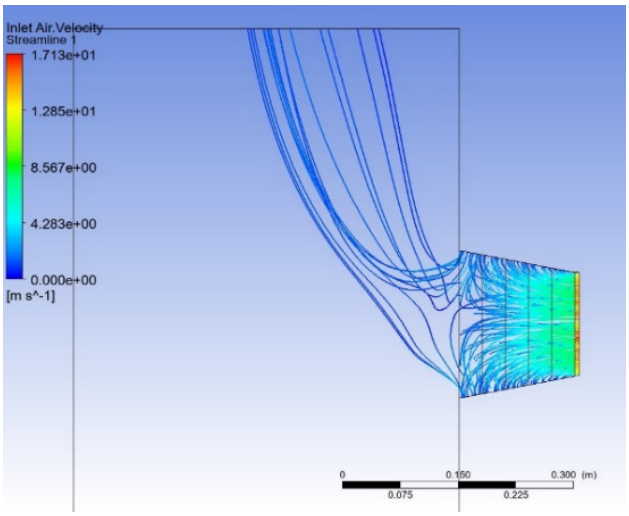

(d) Inlet air velocity contour
for 50°C temperature gradient to aperture

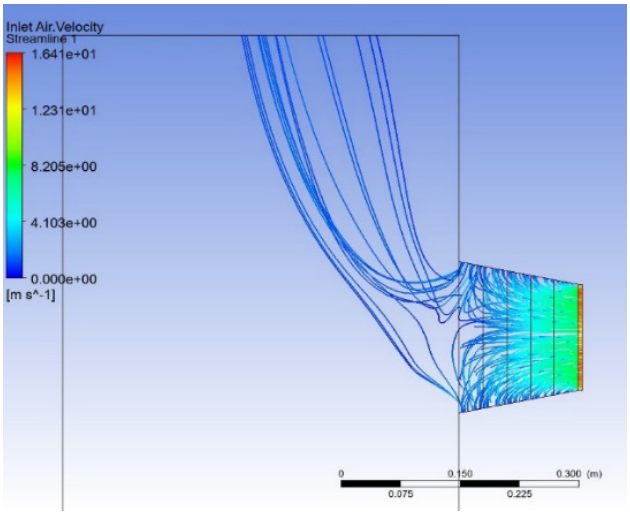

(e) Inlet air velocity contour
for 75°C temperature gradient to the main absorber

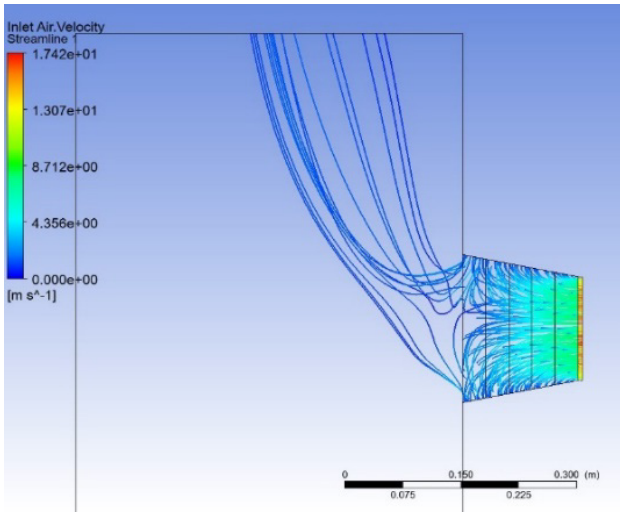

(f) Inlet air velocity contour
for 75°C temperature gradient to aperture

Figure 13. *Comparison of the inlet air velocity contour plots for different temperature gradients*

As previously discussed, in the scenarios illustrated above, the losses to the surroundings exhibit a nearly identical behavior. As a result, it does not affect the ARR in the same manner as changes in geometry or the implementation of mass flow gradients.

Conclusion

The study investigated two distinct approaches. The first approach was developed to find an optimal geometric variation for the receiver in terms of efficiency and subsequently, the aim of the second approach has been to analyze the influence of both mass flow and temperature gradients on it.

The models were generated and assessed within ANSYS environment. Given the relatively straightforward geometry, a structured mesh was employed, aligning well with such configurations. The *k*-omega-SST turbulence model was selected as the most fitting option, given the complexity of the flows being dealt with, as well as its advantageous near-wall treatment capabilities.

ARR represents the fraction of air redirected back into the system after being expelled or discharged. Investigations have showed that the ARR of the receiver is proportional with the efficiency of the receiver since a larger proportion of warm air is effectively reused.

Various analyses have been conducted to enhance the efficiency of the receiver. The model has shown that the pivotal factor in increasing ARR primarily depends on the depth of the receiver aperture. A transition from 50 mm to 150 mm in depth leads to an increase in ARR by 7.83%, and afterwards it shows a decrease of 0.3% as the depth reaches to 200 mm.

Furthermore, assessments of receiver performance encompassed the examination of the rate of change of air inlet mass flow and the response to a rate of change in temperature along the walls of the receiver. These analyses were conducted in both directions, focusing on both the main absorber and the receiver aperture. The comparative examination of the mass flow gradient reveals that increasing the load condition results in a higher ARR, exerting a more substantial impact compared to the orientation of the applied mass flow gradient. However, altering the loads brings about distinct operational states for the receiver since it leads to different air temperatures. As a result, conclusions will be drawn based on constant load variations.

The direction in which the mass flow gradient is applied becomes notably more influential as the proportion of the gradient is increased. For instance, with a 50% mass flow gradient, an ARR enhancement of 1.4% can be achieved when a higher gradient is applied in proximity to the main absorber. This underscores the significance of properly managing mass flow within the receiver system.

Analyses of temperature gradients indicate that introducing such gradients has lower impact on the distribution of ARR under equivalent loads. The applied temperature gradient does affect the flow distribution near the inlet walls but its influence on the internal regions of the receiver is minimal. As a result, it has limited effect on the convective heat losses because it effects on the buoyancy forces and the ARR remain limited.

Upon gathering the collected results, it becomes evident that an observation regarding the ideal configuration of the receiver and the gradients to be employed can be formulated. The receiver attains its highest ARR at full load when possessing a depth of 150 mm. By incorporating a mass flow gradient into the receiver, efficiency can be further elevated by up to 0.21% when the gradient is progressively applied closer to the main absorber. Notably, at this stage, applying a temperature gradient did not exhibit any noticeable influence on the ARR.

Declaration of competing interest

The authors declare that they have no known competing financial interests or personal relationships that could have appeared to influence the work reported in this paper.

References

[1] Khan, I.M., Asfand, F., Al-Ghamdi, S.G. (2023). *Progress in research and technological advancements of commercial concentrated solar thermal power plants.* Solar Energy. doi.org/10.1016/j.solener.2022.10.041.

[2] Pitz-Paal, R. (2020). *19 – Concentrating Solar Power.* Future Energy (Third Edition). doi.org/10.1016/B978-0-08-102886-5.00019-0.

[3] Stadler, H., Maldonado, D., Offergeld, M., Schwarzbözl, P., Trautner, J. (2019). *CFD model for the performance estimation of open volumetric receivers and comparison with experimental data*. Solar Energy. doi.org/10.1016/j.solener.2018.11.068.

[4] Romero M., Steinfeld, A. (2012). *Concentrating solar thermal power and thermochemical fuels*. Energy & Environmental Science. doi.org/10.1039/c2ee21275g.

[5] Zhang, W., Xie, P., Li, Y., Teng, L., Zhu, J. (2022). *3D CFD simulation of the liquid flow in a rotating packed bed with structured wire mesh packing*. Chemical Engineering Journal. doi.org/10.1016/j.cej.2021.130874.

[6] Cagnoli, M., Froio, A., Savoldi, L., Zanino, R. (2019). *Multi-scale modular analysis of open volumetric receivers for central tower CSP systems*. Solar Energy, 190, 195–211. doi.org/10.1016/j.solener.2019.07.076.

[7] Xijie, S., Yongyao, L., Liu, C., Zhengwei, W., Yan, J. (2023). *Numerical simulation and experimental study on an innovative vortex eliminator using a modified SST turbulence model for gas-liquid two-phase flow*. Ocean Engineering. doi.org/10.1016/j.oceaneng.2022.113383.

[8] Cheilyko, A., Göhring, F., Wieghardt, K. (2022). *Receiver efficiency as a determining criterion for the effectiveness of a solar tower*. International Conference on Science, Technology and Management (ICSTM – 2022), 23-24 Nov 2022, Paris, France.

[9] Springer VDI Heat Atlas. (2010). *B1 Fundamentals of Heat Transfer*. In: VDI Heat Atlas. doi.org/10.1007/978-3-540-77877-6.

[10] Cheilytko, A.O. (2014). *Use of secondary energy resources: a study guide for students of ZGIA, specialty 6.050601.* Heat and Power Engineering, full-time and part-time. Zaporizhzhia: ZGIA, 2014. 246 p.

[11] Rodriguez, J.I., Mills, A.F. (1996). *Heat transfer and flow friction characteristics of perforated-plate heat exchangers*. Experimental Heat Transfer. doi.org/10.1080/08916159608946529.

Acknowledgements

The authors would like to thank Kai Wieghardt of DLR for making this research possible, as well as for his support and inspiration.

Yurii SNIEZHKIN, Zanna PETROVA
Leonid VOROBIOV, Anton PETROV
Yuliia NOVIKOVA
Institute of Engineering Thermophysics of the National Academy of Sciences of Ukraine,
bldg. 2, Marii Kapnist Str., 2a, Kyiv, 03057, Ukraine
Corresponding author: bergelzhanna@ukr.net

Doi: 10.53412/jntes-2023-3-3

DRYING OF COMPOSITE RAW MATERIAL BASED ON PEAT SOLID RESIDUE AFTER EXTRACTION OF HUMIC FERTILIZERS AND CORN CROP RESIDUES

Abstract: *The article presents studies of the drying kinetics of composite raw materials based on solid peat residues after extraction of the humus component and corn harvesting residues. The resulting heat of combustion of composite raw materials is 1.2-1.4 times higher than that of peat in its native state. Moreover, their fairly high calorific value allows them to be used as an alternative fuel in domestic and municipal energy.*

Keywords: *peat, corn crop residues, drying.*

Introduction

The task of human development is to preserve the environment and rational use of raw resources. Hydrocarbon fuel and gas are raw resources that are limited and to a large extent exhausted, and their use leads to pollution of the biosphere. The transition from traditional sources of energy to alternative ones is one of the opportunities to renew the raw material base and preserve the ecological situation in the world.

Sources of alternative fuel include peat, biomass, slag and waste from industry, agriculture, utilities and other enterprises.

Peat occupies a special place among natural resources classified as alternative fuels. In Ukraine, most swamps are peatlands. The latter term is often used for drained bogs, sometimes the peat bog is understood as the peat deposit of the bog, especially during its development [1].

Peat contains a large number of humic substances. Because of this, peat has significant energy and agrochemical potential and is used as a local fuel, as well as raw material for the production of greenhouse and consumer soils and organic fertilizers. Peat fuel is the cheapest and most efficient when transported over short distances. The cost of a unit of energy obtained from peat is 3 times cheaper than the cost of the same energy obtained from natural gas [1].

In the production of humic liquid or solid fertilizers, the humic component is extracted from peat. After extraction, a solid residue remains, which can be used more rationally in the future [2].

In order to use the solid peat residue left after extraction of humates as an alternative fuel, it must be dried, as it has high moisture content. But at the same time, the solid residue of peat has a high ash content of 35-45%, which can be reduced by creating a composite based on it with biomass.

The energy potential of biomass in Ukraine is about 26 million tons/year (solid biomass, liquid biofuel and biogas). The sources of solid biomass are various agricultural residues, the amount of which is about

10.8 million tons/year. The largest component of the theoretical energy potential of the country's biomass is corn crop residues after harvesting the grain and is about 4.18 million tons/year [3].

The purpose of the work is to study the drying of composite raw materials based on solid peat residues and corn crop residues.

Materials and methods

Milled peat and corn crop residues were used for the research. The study of the drying kinetics of the composite material was carried out on an experimental convective stand, which is equipped with an automatic system for collecting and processing information [4].

Results

In order to obtain high-quality material in the drying process, the 100/70°C and 100°C modes were studied. Figure 1 shows the changes in humidity and drying temperature of the mixture based on the solid residue of peat after extraction of the humic component with the crushed corn crop residues at the temperature regimes of 100°C and 100/70°C. As can be seen from Figure 1, the 1-stage drying mode of peat-corn mixture 100/70°C compared to the drying mode of 100°C indicates an increase in the duration of drying by only 9%, but the quality of the material is the same as with the mode. The duration of drying at a temperature of 100°C is 18 min to a humidity of 10%, and at 100/70°C – 42 min to a humidity of 4%, that is why there is such a difference in time.

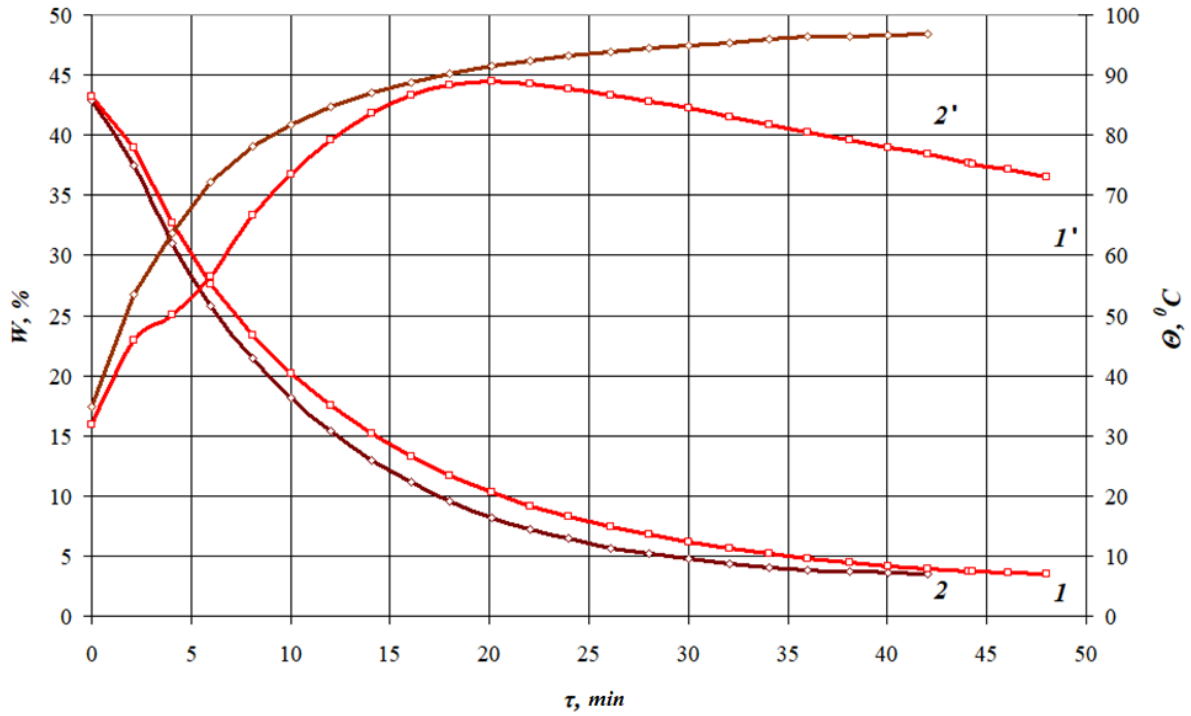

Figure 1. *Change in humidity (1, 2) and temperature in the middle of the layer (1′, 2′) of the mixture based on the solid residue of peat after extraction and the crushed corn crop residues in a ratio of 1:1. Mode parameters: V = 3 m/s, h = 10 mm, particle size ≥0.5 mm: 1, 1′ – 100/70°C; 2, 2′ – 100°C*

Figure 2 presents the curves of the drying speed of the mixture based on the solid residue of peat after the extraction of humid substances and corn crop residues crushed to 0.5 mm. As can be seen from the curves in Figure 2, the maximum drying rate of the mixture at a temperature of 100°C is 3.2%/min, and at a step mode of 100/70°C – 3.3%/min.

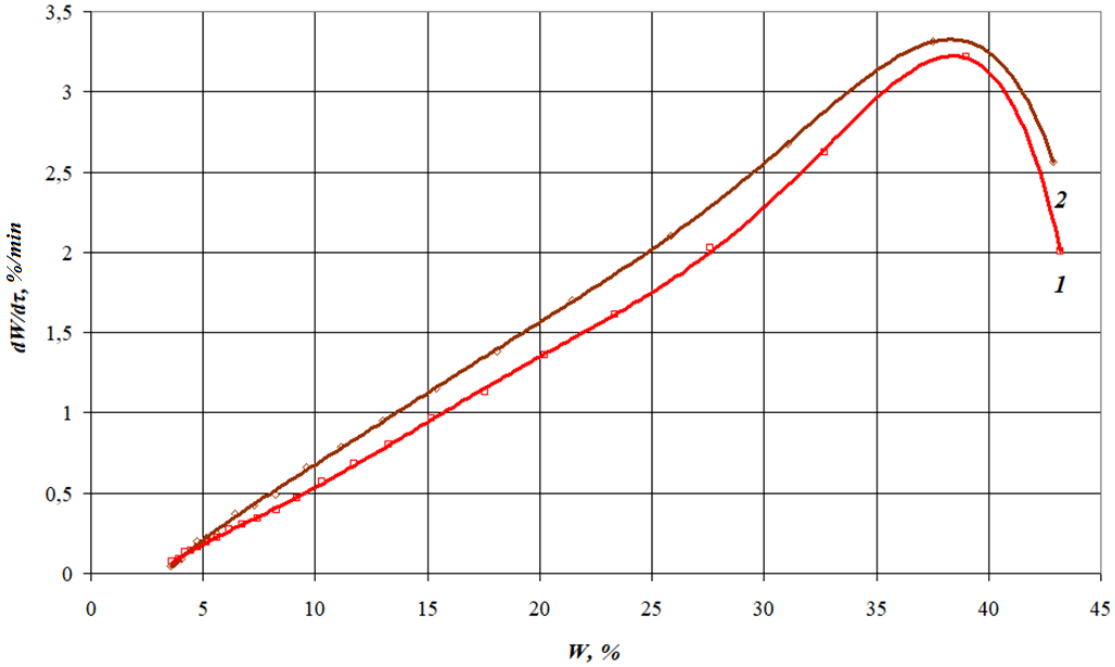

Figure 2. *Change in the speed of the mixture based on the solid residue of peat after extraction and the crushed corn crop residues in a ratio of 1:1: 1 – 100/70°C; 2 – 100°C*

A study of the specific heat of combustion of composite raw materials was carried out. The method of determining the heat of combustion corresponds to the standard method for solid fuel DSTU ISO 1928:2006 and the European standard ISO 18125:2017 "Solid biofuels – Determination of calorific value" [13, 14].

The generalized results of measurements and calculations of the properties of the studied samples in the delivery state and in the dry state are shown in Table 1.

Table 1. *Generalized results of measurements and calculations of sample properties*

Properties	Native Irpin peat	Corn crop residues	Solid residue of peat after extraction Irpin	Solid residue of Irpin peat + corn crop residues 1:1	Chernihiv native peat	Solid residue of peat after extraction Chernihiv	Solid residue of Chernihiv peat + corn crop residues 1:1
Humidity is finite W, %	9.7	8.5	6.2	4.9	16.1	6.6	5.3
Ash content in the delivery state, %	34.9	3.5	34.5	13.7	24.8	26.5	9.4
Dry ash content, %	27.2	3.5	36.8	14.4	24.8	28.3	10.9
Higher heat of combustion in the state of delivery, MJ/kg	12.22	20.67	14.35	16.59	13.50	14.31	16.57
Higher heat of combustion in the dry state, MJ/kg	13.53	21.36	15.30	17.46	16.09	15.33	17.50
Lower heat of combustion in the state of delivery, MJ/kg	11.26	17.78	13.42	15.23	12.33	13.27	15.32
Lower heat of combustion in the dry state, MJ/kg	12.22	17.94	13.99	16.15	14.78	14.02	16.19

As can be seen in Table 1, the content of humates in peat does not affect the heat of combustion of peat. At the same time, it becomes the same regardless of the deposit from which it was mined. As can be seen from the obtained experimental data, the heat of combustion of composite raw materials is higher than that of peat in its native state. Also, a sufficiently high heat of combustion allows them to be used as an alternative fuel in household and communal energy. Table 1 shows their characteristics in the dry state (W = 0%).

Conclusions

The study of the kinetics of the drying process of composite raw materials based on the solid residue of peat after extraction and the remains of corn crop residues made it possible to develop an effective drying regime that improves the quality of the material. The kinetics of the drying process of composite raw materials based on the solid residue of peat after extraction and the remains of corn crops were studied. An effective drying mode has been developed, which improves the quality of the material.

References

[1] Petrova, Zh.O., Pazyuk, V.M., Novikova, Y.P., Petrov, A.I. (2022). *Research on the processing of peat into composite fuel*. In Painted M.S. (Eds.), Sustainable Development: Environmental Protection. Energy saving. Balanced nature management: collective monograph (93-103). Kyiv: Yarochenko Ya.V. [in Ukrainian].

[2] Petrova, Zh.O. (2015). *Study of modes of extraction of humus and humic substances*. Scientific works of the Odessa National Academy of Food Technologies, 47(2), 190-194. [in Ukrainian].

[3] Geletukha, G.G., Zheliezna, T.A., Kucheruk, P.P., Drahniev, S.V. (2023). *Analysis of prospective directions for using Ukraine's biomass potentional for energy*. Thermophysics and Thermal Power Engineering, 45(2), 77-86. https://doi.org/10.31472/ttpe.2.2023.9 [in Ukrainian].

[4] Petrova, Z., Sniezhkin, Y., Paziuk, V., Novikova, Y., Petrov, A. (2021). *Investigation of the Kinetics of the Drying Process of Composite Pellets on a Convective Drying Stand*. Journal of Ecological Engineering, 22(6), 159-166. https://doi.org/10.12911/22998993/137676.

[5] Derzhspozhivstandart. (2008). *Solid mineral fuels. Determination of the highest heat of combustion by the method of combustion in a calorimetric bomb and calculation of the lowest heat of combustion* (DSTU ISO 1928:2006 (ISO 1928:1995, IDT)).

[6] Solid biofuels – Determination of calorific value (ISO 18125:2017). (2017).

Larisa TRETYAKOVA
Liudmyla MITIUK
National Technical University of Ukraine "Igor Sikorsky Kyiv Polytechnic Institute",
Institute of Energy Saving and Energy Management, 37, Prosp. Beresteyskiy, Kyiv, 03056, Ukraine
Corresponding author: lt79@ukr.net

Doi: 10.53412/jntes-2023-3-4

MATHEMATICAL MODELLING TECHNIQUE TO ASSESS SOIL CONDITIONS

Abstract: *This paper analyzes the results of studying contaminated soil samples from a combat zone (Sumy region, Ukraine). The authors proposed a mathematical model for simulating and assessing the impact of military operations on soil and groundwater. The mathematical model will make it possible to predict the occurrence of environmental emergencies and reduce the frequency of expensive experimental studies of soils contaminated with heavy metals.*

Keywords: *heavy metals, soil, groundwater, mathematical model.*

Introduction

The armed conflict that broke out in Ukraine in 2014 caused environmental problems associated with the accumulation of pollutants in soil and water bodies. Between 2014 and 2021, about 50,000 square kilometres have been affected in Ukraine due to hostilities. A study of the soil surface in the conflict zone was conducted in 2014 under OSCE support. The study found a 1.2–12-fold increase compared to the background levels in heavy metals content in most of the soil samples taken from the areas of hostilities. Mercury, vanadium and cadmium concentrations were consistently 1.1–1.3 times higher than the normal levels. The highest content of heavy metals was found in the areas of shell bursts. Since the beginning of Russia's full-scale invasion of Ukraine (February 24, 2022), these areas have grown significantly (up to 150–180 thousand sq km) with an significant increase in the consequences for the ecosystems.

According to open sources, the armed aggression has polluted more than 3% and contaminated up to 10% of Ukrainian land, causing up to UAH 500 billion in damage. Landmines represent a separate type of contamination. According to the Ukrainian Deminers Association, an area of more than 80.5 thousand sq km (14%) of Ukraine's territory is mined. Such lands (soils) have been removed from economic use, in part or whole, until complete mine clearance [1].

As the international experience shows, armed conflicts significantly impact properties of soil health, disrupting some of its physical and chemical properties and causing contamination, which is especially dangerous for agricultural lands. Direct hits by shells, burnt-out military equipment and oil products, destroy ecosystems and cause soil and water to become contaminated with heavy metals and toxic elements. The most hazardous soil pollutants are lead, mercury, arsenic, cadmium, copper, nickel and zinc. During military operations, these and other heavy metals are released into the surrounding environment from firearms remnants with mixtures of metal-containing particles. Metal residues are one of the most dangerous consequences of military actions, and they generally persist for the longest time in the areas of hostilities.

Potentially toxic elements in the war-affected areas include lead and related contaminants – antimony, chromium, arsenic, mercury, nickel, zinc and cadmium. The explosives also contain large amounts of mercury. Zinc, copper, nickel, lead and chromium are used to coat bullets, missiles, gun barrels and military vehicles. Barium, stibium, bismuth, and boron are standard charging compounds in weapons, and tungsten is used in aerial bombs. Once released into the environment, potentially toxic elements of the ammunition get oxidised upon contact with air, and their residues enter the soil, where various chemical processes occur.

To determine the impact of hostilities on the soil surface after the liberation of Sumy Oblast in 2022, experts took samples at the sites of bomb drops and in demined areas. The results showed that the contents of the following metals exceeded the maximum allowable concentrations: lead – in 60% of soil samples (1.4 to 10.6-fold); copper – in 50% of samples (1.1 to 6.1-fold); zinc – in 20% (1.3 to 3.4-fold); manganese – in 20% (2.3 to 2.4-fold). The soil samples' total content of heavy metals exceeded the background levels by 1.1–5.4 times. The study revealed the highest levels of lead and the lowest levels of iron [2].

The global experience of post-war territory clearance shows long-term demining, reclamation and decontamination of such lands. Given the particular density of mining and artillery shelling, such processes will require significant workforce and financial resources.

Since extensive soil and water chemical contamination is expected, ensuring an effective environmental monitoring system after the war is essential. Such monitoring will make it possible to determine the actual degree of ecological damage and implement timely and effective measures to prevent further deterioration and restore safe ecosystems for both people and animals.

Purpose and research goals

Currently, experimental research methods cannot be used because of the ongoing shelling throughout the country. A possible solution to this problem is to develop a method for predicting potential soil and groundwater contamination levels using mathematical models.

Materials and Methods

When developing a general algorithm for assessing the environmental impact of hostilities, it is recommended to collect the following information in advance:

- on the use of certain types and kinds of ammunition, shells, missiles, and aerial bombs on the studied territory;
- on the mining of the territory and the possibility or impossibility of its complete clearance;
- on the impact on local features from the destruction of unexploded ordnance that cannot be neutralised and can only be eliminated in situ by detonation;
- on the surface condition, as explosions can alter the topography of the territory and move soil layers.

A method has been proposed for modelling the spread of heavy metal salts deep into the soil in contaminated areas. Such modelling aims to estimate the likelihood and timing of emergencies.

Heavy metals from ammunition and military equipment end up in the soil and groundwater. The first type of emergency occurs with deep soil salinisation. The second type of emergency arises when molecules of heavy metals enter the water table. The modelling of the movement of heavy metal molecules in multilayer soils involves several stages. The initial prerequisite for developing the mathematical model field is the presence of chemical compounds of heavy metals in the surface soil at concentrations exceeding the allowable levels.

$$\rho_i^d\left(x_0, y_0, z_0, t\right) \geq PC_i \tag{1}$$

where:

ρ_i^d – concentration of the dangerous substance;

x_0, y_0, z_0 – initial coordinates of the source of pollution;

PC – permissible concentration;

i – chemically dangerous compound that has reached its limit (permissible concentration).

The movement of heavy metals occurs in the aeration zone, and different territories will have different rates of contamination spread.

The nonlinear nonstationary model uses an equation from the theory of physicochemical fluid dynamics in porous media [3].

$$D_m(\theta)\frac{d^2C}{dX^2} = \theta\frac{dC}{dT} \tag{2}$$

where:

$D_m(\theta)$ – molecular diffusion coefficient, m²/s;

C – salinity of the soil (rocks), %;

Θ – volumetric humidity, %;

X – spatial coordinate, m;

T – time coordinate, s.

It should be noted that these values are probabilistic and depend on the structure of the aeration zone, the properties of metal molecules, temperature, pressure, humidity and substance concentration.

The analytical solution of equation (2) has the form:

$$C_{hx} = \left(C_s - C_0\right) erfc\left[\frac{1}{2}\cdot\frac{h_x}{\sqrt{\frac{D_m(\theta)\cdot t}{\theta}}}\right] \tag{3}$$

where:

C_{hx} – predicted salinity level at h_x depth, %;

C_s – surface salinity of the aeration zone at (x_0, y_0, z_0) surface points at h = 0;

C_0 – the initial level of salinity at (x_0, y_0, z_0) points on the surface of the soil before storage at t = 0;

h_x – distance of the calculation points from the (x_0, y_0, z_0) surface points, i.e. from the earth's surface, m;

t – term of prediction calculation, day;

$erfc$ – tabulated function.

The risk of emergencies and assessment of potential consequences are provided as additional boundary conditions in the model:

- an emergency caused by an increased deep soil salinisation

$$C_x < q\left(C_x, t, h_x\right) < 0.35 \tag{5}$$

- an emergency caused by the penetration of a chemically hazardous compound containing heavy metals into subsurface or groundwater

$$h_0 \le q\left(C_x, t, h_x\right) \le H \tag{6}$$

where:

h_x – depth of penetration of chemically hazardous compounds into the soil;

$q(C_x, t)$ – an indicator that further determines the nature of the spread of danger and is a reflection of the sources of danger;

H – depth of the aquifer within the territory of possible distribution.

The model is based on the following assumptions: metal accumulation is cumulative; salt transfer occurs during free penetration and normal infiltration; soil humidity is characterised by seasonal fluctuations (winter-spring and summer-autumn).

To apply the modelling method, it is necessary firstly to assess experimentally the concentration of hazardous substances, the depth of their penetration and the structure of the aeration zone, which may have changed due to shelling and explosions. The values of other variables used in the formulas can be obtained from the literature.

Conclusion

A mathematical model has been proposed for modelling and assessing the impact of hostilities on soil and groundwater. Based on the modelling results, predicting the time of environmental emergency occurrence is possible. This method can significantly reduce the need for expensive experimental research and determine the priority of land revegetation in different parts of the country.

References

[1] Website of the Ukrainian Deminers Association URL: https://www.uda.org.ua/.

[2] Zaitsev, Y.O., Gryshchenko, O.M., Romanova, S.A., Zaitseva, I.O. (2022). *Influence of military operations on the content of gross forms of heavy metals in the soils of Sumy and Okhtyrka districts of Sumy region*. Agroecological journal, 3, 136–149. doi.org/10.33730/2077-4893.3.2022.266419.

[3] Tretiakova, L., Panasiuk, I., Mitiuk, L., Rebuel, E. (2022). *Method for predicting the dissemination of hazardous substances in the soil during long-term storage of galvanic waste*. EUREKA: Physics and Engineering, 1 (38), 12-22. doi:10.21303/2461-4262.2022.002231.